COMPUTATIONAL IMPACT PRESSURE OF THE FLOATPLANE'S BOTTOM IN VARIOUS OF DEADRISE AND FLARE ANGLES

Aries Sulisetyono*, Zambilly A. Washoya, Achmad Zubaydi

Department of Naval Architecture, Institut Teknologi Sepuluh Nopember, Kampus ITS Sukolilo, Surabaya, Indonesia
*sulisea@na.its.ac.id

The water impact at the bottom of a floatplane upon landing is one of the biggest concerns related to the structure strength. The free fall of the floater to the water's surface is ideal for modelling to acquire a pressure value against the optimal design angle of the deadrise and flare. The impact pressure due to free-falling of the 2D cross-section of the floater at four different deadrise angles is computed using the computational fluid dynamics (CFD) technique in FLUENT's dynamic mesh feature. According to the simulation results, the angle of deadrise impacts the pressure on the floater bottom area that decreases along with the increase in deadrise angle. Flares also help to lessen the pressure value under all deadrise angle scenarios. All models have good agreement when compared to the modified Wagner's formula, with an average inaccuracy of roughly 5.27 percent.

Keywords: floatplane,free fall, impact pressure, deadrise angle, flare

1   INTRODUCTION

An impact pressure must be considered in a floatplane's floater design when the floatplane begins to touch the water's surface during landing. The structural damage that may occur because of the floatplane landing process must be evaluated due to the impact pressure on the floater's lower plate [1]. During the landing phase, a pilot keeps the floatplane's height above the water level as low as possible before dropping it using the free fall body concept [2]. The floatplane's landing on the water's surface is disrupted under some conditions, such as bad weather; especially, a floatplane may suffer a drop from a very high height, and an initial speed may also appear when a floatplane is in free fall. Previous researchers used analytical methods, model experiments, and numerical simulation to study free-falling objects with the goal of estimating the pressure load received by the body's bottom hitting the water surface.

In most cases, a free-fall body is studied in two and three dimensions. However, the approach based on an assumption of a two-dimensional model is the most generally employed, but in circumstances when a body trim is required, a three-dimensional model should be utilized [3]. Karman [4] was a pioneer in the study of free-falling objects on the water's surface, in which a two-dimensional object falls freely at a constant speed. Wagner [5] proposed a study of slamming by observing the rise in water or spray that occurs when a blunt object falls freely to the calm water at a steady speed. The equation derived by Chuang [6] on a blunt item in six variations of the deadrise angle was used to solve the impact body owing to slamming. Similarly, in the case of different deadrise angles, solve the free-fall wedge to the water surface using the Wagner equation [7]. Greenhow [8] devised another equation, although it is only applicable to deadrise angles greater than 60 degrees. The topic of a slamming body in water has been the subject of some review study [9, 10].

The impact pressure of a free-falling body with a deadrise angle of 4 to 81 degrees was calculated analytically, with the minimum and maximum pressures appearing at deadrise angles of 20 and 81 degrees, respectively [11]. Maximum pressure is found near the spray root area at a deadrise angle of 20 degrees, whereas with a deadrise angle of more than 45 degrees, maximum pressure occurs in the keel area [12]. Experiments on a two-dimensional cross-sectional model to determine the impact pressure at the seaplane's bottom yield findings that are very close to those obtained using the modified Wagner equation [13]. Other free-fall wedge models were also tested in the water tank, with the results being used to validate the results of numerical simulations by demonstrating good agreement [14]. The effect of mass, gravity, deadrise angle, and initial velocity on impact pressure was then examined.

The finite element method was adopted to quantitatively simulate the slamming of a 3D-wedge on the sea surface using the LS-DYNA software [15]. Using CFD methodologies such as the fluid volume method (VOF) and the global moving mesh method (GMM) to deal with the free fall motion of the wedge, approximate solutions for the impact under varied free fall speeds of the wedge were assessed [16]. The numerical wave tank (NWT) of OpenFOAM was used to generate the overset-mesh to model the water entrance of the 2D symmetric or asymmetric wedge body into the regular wave [17]. Previous research has shown that the form of a floater's bottom shape affects impact loads when it reaches the water's surface. The presence of flares, on the other hand, may lessen the impact pressure on the floater's bottom plate since flares can produce a lesser spray as the floater enters the water. Flare angles in the range of 1–2 degrees can provide significant benefits [18].

Aries Sulisetyono, et al. - Computational impact pressure of the floatplane's bottom in various of deadrise and flare angles

Journal of Applied Engineering Science- Vol.20, No 3, 2022 -www.engineeringscience.rs

This research discusses the pressure load that occurs during floatplane landing operation on the newly introduced floater design [19,20]. FLUENT software and the modified Wagner's equation are used to solve a two-dimensional sectional of the floater falling freely onto the sea surface. The impact pressure on the floater's bottom plate is compared to the differences in deadrise angles and flares at varied initial values of falling speed and height.

2 METHODOLOGY

The floater is being developed with the intention of converting a standard N219 aircraft into an amphibious or float plane. The floater is designed to find the smallest feasible resistance force and minimize the impact pressure caused by the floatplane landing on a calm water surface. The resistance force and impact pressure can be reduced by setting proper deadrise and flare angles on the bottom floater. It is not linear, as a body with a low angle of deadrise might produce a low resistance force but a high impact pressure, while the opposite of a high deadrise angle produces a low impact pressure. Alternatively, flares may lower the impact pressure and lessen the spray [18].

The numerical approach of CFD is proposed in this case to analyze the impact pressure that arises at the bottom of the floater when it collides with the calm water surface. Figures 1 and 2 demonstrate the floater design in three-dimensional form as the line plan, with views of the body plan and the sheer plan, respectively [21]. The longitudinal body is made up of two portions, the fore and after bodies, which have differing body forms. It has 12 stations, six in the after-body and six in the fore-body, as indicated in the basic plan in Fig. 2. Station 5 has two numbers labeled "St 5A" and "St 5F," respectively, at the bottom and top of the transverse steps. The after-body section's deadrise is shaped like a line, whereas the fore-body section's deadrise is concave. Figure 3 depicts the floater's symmetrical two hull catamaran with the primary dimensions listed in Table 1.
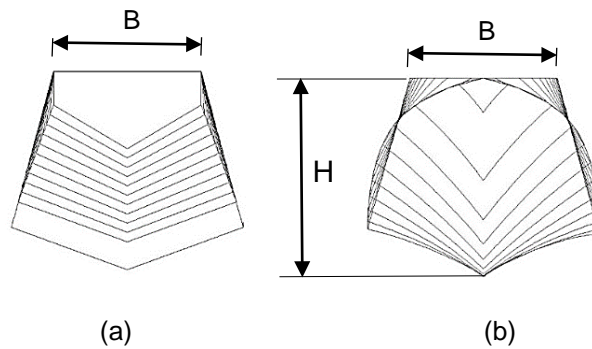

(a)   (b)
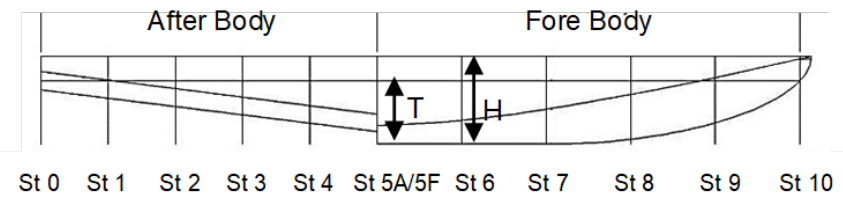
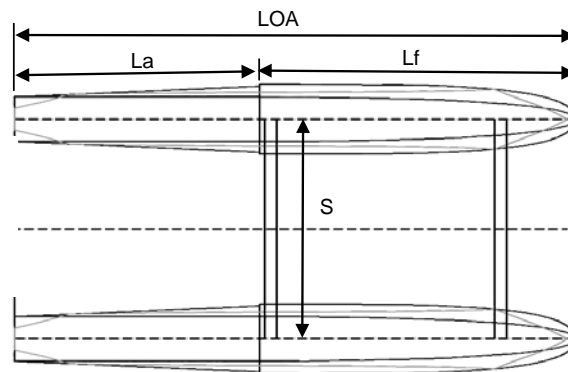Fig. 1. Body plan of (a) after and (b) fore body

Fig. 2. Sheer plan in 12 stations

Fig. 3: Half-breadth plan

Aries Sulisetyono, et a.l - Computational impact pressure of the floatplane's bottom in various of deadrise and flare angles

Journal of Applied Engineering Science- Vol.20, No 3, 2022 -www.engineeringscience.rs

Table 1. The main dimensions of the LNG ship

Item	Value
Length Overall (LOA)	9.40 m
Length Between Perpendiculars (LBP)	9.27 m
Breadth of Demihull (B)	1.25 m
Height (H)	1.07 m
Draught (T)	0.77 m
Space Between Demihull (S)	3.95 m
Forebody Lenght (Lf)	5.30 m
Afterbody Length (La)	4.10 m
Displacement (Δ)	7.33 ton

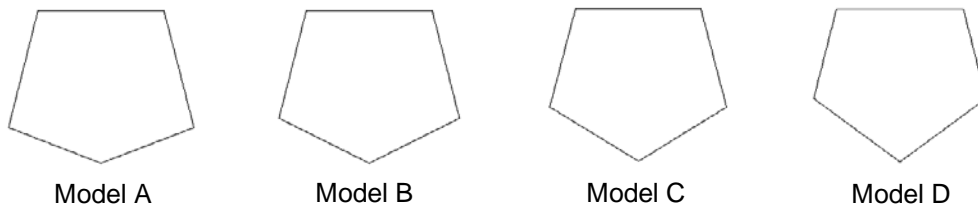Model A   Model B   Model C   Model D

Fig. 4. Cross section of models at station 5A

Model A, which has a 20-degree deadrise angle in the after-body portions, is the floater's section depicted in Fig. 2. When deadrise angles are added to model A, the other models B, C, and D are created, becoming 25, 30, and 35 degrees, respectively. On model A, altering the deadrise angle necessitates raising the draft height in order to maintain the same displacement of the floater. Model A has only been modified in after-body stations with varied widths but the same deadrise angle, such as stations 0 to 5A. The section of the forebody is not changing as defined by model A. Figure 4 shows the cross-section of all models for a case of station 5A on the after-body as an example.

Reynolds-averaged Navier-Stokes (RANS) method is an acceptable method in CFD applications for solving flow problems with the governing equations (1) and (2), represented in a cartesian tensor form as,

$$\frac{\partial \rho}{\partial t} + \frac{\partial}{\partial x_i}(\rho u_i) = 0 \tag{1}$$

$$\frac{\partial}{\partial t}(\rho u_i) + \frac{\partial}{\partial x_j}(\rho u_i u_j) = -\frac{\partial p}{\partial x_i} + \frac{\partial}{\partial x_j}\left[\mu\left(\frac{\partial u_i}{\partial x_j} + \frac{\partial u_j}{\partial x_i} - \frac{2}{3}\delta_{ij}\frac{\partial u_l}{\partial x_l}\right) + \frac{\partial}{\partial x_j}\left(-\rho\overline{u_i' u_j'}\right)\right] \tag{2}$$

Where u_i denotes the components of velocity (i= 1, 2, 3), ρ denotes density, p denotes pressure, and $-\rho\overline{u_i' u_j'}$ denotes Reynolds stresses. Fluid flow is assumed to be transient to resemble real-world situation. In fluid modelling of a free surface, the fluid volume approach (VOF) is used. The fluid transport equations (3) and (4) are used to compute the turbulence model's kinetic energy, k, and its rate of dissipation, ε.

$$\frac{\partial}{\partial t}(\rho k) + \frac{\partial}{\partial x_i}(\rho k u_i) = \frac{\partial}{\partial x_i}\left[\left(\mu + \frac{\mu_t}{\sigma_k}\right)\frac{\partial k}{\partial x_j}\right] + G_k + G_b - \rho\varepsilon - Y_M + S_k \tag{3}$$

$$\frac{\partial}{\partial t}(\rho\varepsilon) + \frac{\partial}{\partial x_i}(\rho\varepsilon u_i) = \frac{\partial}{\partial x_i}\left[\left(\mu + \frac{\mu_t}{\sigma_\varepsilon}\right)\frac{\partial\varepsilon}{\partial x_j}\right] + C_{1\varepsilon}\frac{\varepsilon}{k}(G_k + C_{3\varepsilon}G_b) - C_{2\varepsilon}\frac{\varepsilon^2}{k} + S_\varepsilon \tag{4}$$

Where G_k and G_b are the turbulence kinetic energy and buoyancy, respectively, generated by the mean velocity gradient and buoyancy. The overall dissipation rate is affected by the variable dilatation of incompressible turbulence which is represented by Y_M. $C_{1\varepsilon}$, $C_{2\varepsilon}$, and $C_{3\varepsilon}$ are constants. The turbulent Prandtl numbers for k and ε, are σ_k and σ_ε, respectively. S_k and S_ε are source terms that have been defined by the user.

The boundary condition configuration shown in Fig. 5 quantitatively explains the issue area. The floater's surface is shown by the selected body line, and the moving fluid is pointed at the moving fluid area. The pressure outlet component is defined as the outlet line, and the fluid barrier is defined as the tank wall. The simulation duration is transitory, with gravity in the *y*-direction of 9.81 m/sec2. The flow model is multiphase (water and air with viscosity),

Aries Sulisetyono, et al. - Computational impact pressure of the floatplane's bottom in various of deadrise and flare angles

Journal of Applied Engineering Science- Vol.20, No 3, 2022 -www.engineeringscience.rs

and the flow is turbulent (*k*-epsilon model). Using CFD's dynamic mesh capability, objects can migrate from one boundary condition to the next within a single zone. It not only creates the moving object, but it also allows the dynamic mesh setup to update the mesh based on movement, ensuring that there are no mesh distortions while the object is moving. Under the six DOF motions of the body, the smoothing mesh with re-mesh is chosen. Then the UDF (User Defined File) is developed to be compiled in FLUENT.
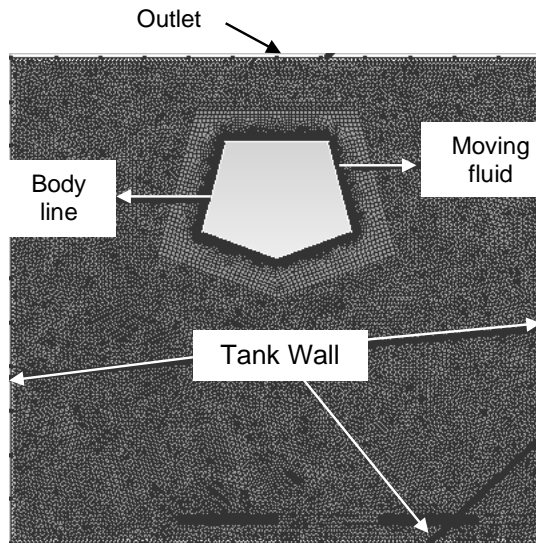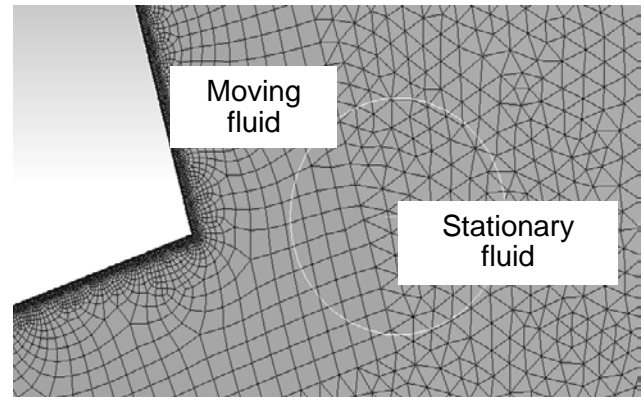

Fig. 5. Boundary condition

Fig. 6. Type of Meshing

In modeling, the 2D drawing of each model is exported to the modeler application GAMBIT for the mesh generation. The two methods of mesh generation include the multi-zone and the triangle. The multi-zone method is suitable to handle the fluid moving around the solid body, and the triangle mesh presents a stationary fluid. Figure 6 shows the two-surface meshing area which commits to the stationary fluid and the moving fluid. The face and the edge size are considered on both the water surface and the wall, respectively. The mesh form is getting tighter on the wall area, and both the surface area and the mesh connection group relate to the mesh connection group to avoid distortion during simulation. The number of meshes or elements utilized in simulation refers to the outcome of an independent mesh study that attempts to accurately carry out simulation results. The optimal mesh number is studied with a focus on lowering computational error and the computational process's time-consuming nature. The number of meshes starts at 8443 and gradually rises to 1.5 times that of the previous mesh. The mesh number is added until the difference between the results in terms of static pressure is less than 2% after the mesh number has been added. The ideal meshing number, according to Table 2, is around 27164, with a difference of 1.83 percent.

Table 2. Grid independence results

Number of Element	Pressure (Pa)	Difference
8443	269426	12.20%
12285	236545	16.71%
18634	197020	17.06%
27164	163415	1.83%
40540	166400	

The floatplane's landing procedure is essentially the same as that of a conventional airplane: the floatplane lowers to the water's surface as low as possible before being released as a free-falling body. In bad weather, a pilot may have trouble keeping a floatplane's height over the free surface. As a result, the free-fall floater simulation is carried out at two different initial heights, 0.5 m and 1 m above the ocean surface. The floater's free-fall velocity is affected by its initial altitude. In free-fall situations, initial velocities of 0 m/s and 5 m/s are also investigated. The floater's free-fall velocity, *Vt,* may be estimated using the free-fall motion theory by removing the inhibiting air friction force, as in (5) [22].

$$Vt = Vo + \sqrt{2gh}$$
(5)

Where *Vo* denotes the initial velocity of the free fall floater, *g* denotes the acceleration due to gravity, and *h* denotes the vertical height of the floater at start position. In this study, four combinations of initial velocity and altitude are considered to check the sensitivity of initial values. For a free fall case of model A, the differences in the results of

Aries Sulisetyono, et a.l - Computational impact pressure of the floatplane's bottom in various of deadrise and flare angles

Journal of Applied Engineering Science- Vol.20, No 3, 2022 -www.engineeringscience.rs

all combinations are up for discussion. The inclusion of a flare on a floater was found to lessen the impact load [18]. The effect of flare on pressure values is investigated by contrasting two body states with and without flare. Figure 7 illustrates the model with a deadrise angle and no flare angle, β, and the model with an additional flare angle, θ. Flares at varying angles are present in all portions of the forebody design, as shown in Fig. 1b. The addition of flares to the floater enhances the lift force and reducing resistance forces. There are six different deadrise angles and flares in the forebody at stations 5F to 10, ranging from 20 to 48 degrees and 24 to 52 degrees, respectively. The impact of six flare angles on pressures arising when a floater free falls from a height of 0.5 meters without a beginning speed is discussed in this paper. The best combination of deadrise and flare angles for reducing impact pressure has been identified.
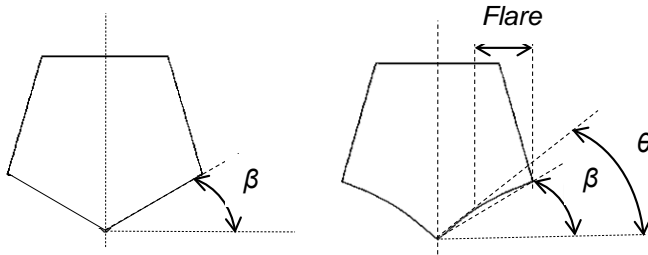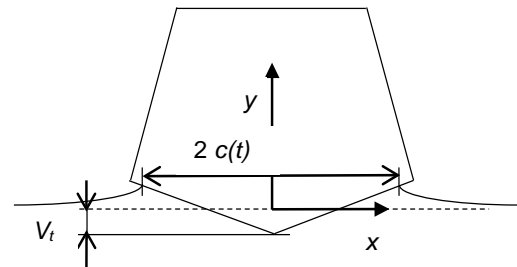
Fig.7. Models of unflared and flared body   Fig.8. Model of floater entry into water

The accuracy of the CFD approach must be verified by comparing the CFD results against the computation of the modified Wagner equations in the scenario of free fall into the water. The modified Wagner equation was developed mostly by modeling the wedge entry into calm water (see Fig. 8).Faltinsen [12] established the boundary-value problem as a simplified analysis that evaluated the velocity potential in the situation of a two-dimensional body free falling onto the calm water. Body boundary conditions that do not need flow through the body surface are converted to a straight line, $x = 2\,c(t)$,using the Taylor series expansion.The Euler equation, which is the foundation for deriving the Bernoulli equation, is solved in calm water with no forces and no atmospheric pressure. The expression of the equation was used to determine fluid flow in terms of a complex equation, which was then used to estimate velocity potential and pressure (6).

$$p - pa = \rho V \frac{c}{(c^2 - x^2)^{\frac{1}{2}}} \frac{dc}{dt} + \rho \frac{dV}{dt}(c^2 - x^2)^{\frac{1}{2}}$$
(6)

where p stands for pressure. V is a submerged body's vertical velocity, obtained from the lowest point of body to the line of calm water. $V$is taken to be a constant, similar to the free-fall speed of objects specified by (5). When the object sinks, c is the water level length at half its breadth.

The floater structure design regulation includes important seaplane airworthiness criteria set by the Code of Federal Regulations (CFR) [23]. Water loads created when landing with the seaplane in any attitude expected to occur in normal operation at an acceptable sinking velocity in the most severe sea conditions likely to be encountered must be designed into the structure of the seaplane. The water load criteria must be met at each operating weight, up to the design landing weight. Each float on a twin-float seaplane must be viewed as an analogous hull on a fictitious seaplane with a weight equal to one-half of the twin-float seaplane's weight. For the step landing case, the water reaction load factor, n_w, must be calculated with Eq. (7) [23]:

$$n_w = \frac{C_1 V_{SO}^2}{(\tan^{2/3} \beta) W^{1/3}}$$
(7)

where C_1 is the empirical seaplane operations factor equal to 0.012. $V_{SO}$is the stalling speed of a seaplane in knots, with the flaps extended in the proper landing position and no slipstream influence. $\beta$and Wdenote deadrise angle and landing weight, respectively. Using Eq. (7), the load factors of twin models A, B, C, and D are calculated to be 4.22, 3.58, 3.10, and 2.73, respectively, which are all higher than the Federal Aviation Administration's minimal step load factor of 2.33 [23]. The following local pressure distributions must be used in the design of the bottom plating and stringers, as well as their connection to the supporting structure. The local pressure at the keel (psi) is calculated as follows: Eq. (8) for an unflared bottom [23].

$$P_K = \frac{C_2 K_2 V_{SO}^2}{(\tan \beta)}$$
(8)

where C_2 is 0.00213 and K_2 is the step hull section's weighting factor, which is 1. Using Eq. (8), the maximum pressure requirement of the floater design is determined in line with the Federal Aviation Administration's rule [23],

Aries Sulisetyono, et al. - Computational impact pressure of the floatplane's bottom in various of deadrise and flare angles

Journal of Applied Engineering Science- Vol.20, No 3, 2022 -www.engineeringscience.rs

which is found to be roughly 126.41 kPa, 98.67 kPa, 79.69 kPa, and 65.71 kPa, respectively, for the design of models A, B, C, and D.

3 RESULTS AND DISCUSSIONS

The results of the free-fall simulations of models A, B, C, and D in terms of maximum pressure at each station along the afterbody are shown in Fig. 9. Figure 10 shows the forebody's station simulation results under an unvarying deadrise angle (model A). These simulations are run at a speed of Eq. (5) with no initial speed, V_o, and a height of about 0.5 m above the sea surface, h.
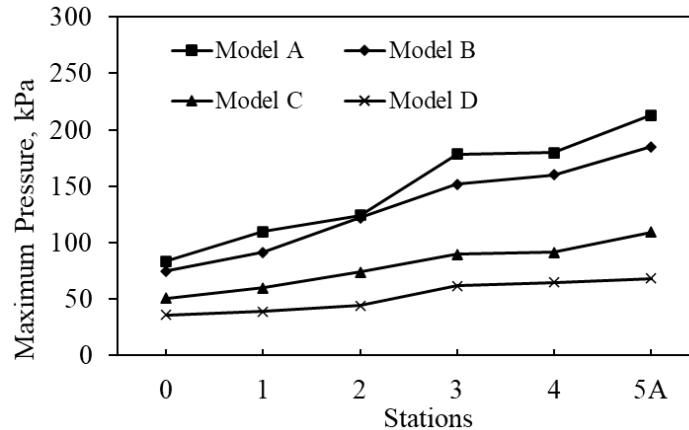

Fig. 9. Maximum pressure of model A, B, C, and D in after body

The linear increase in pressure from station 0 to the transverse step station 5A of model A is depicted in Figure 9. The maximum pressure is found at station 5F, then drops exponentially towards station 10 as illustrated in Fig. 10. The curves' tendency is nearly identical for additional models B, C, and D with varying pressure values. It appears that the width of the bottom hull in the after body increases linearly from station 0 to 5A, while the width of the forebody opposite has steadily decreased from station 5F to 10 (see Fig. 3). Another reason is that the flared region of the forebody differs from the afterbody without flares. Longitudinally, the highest impact pressure is found in the midship area, at station 5F, followed by station 5A, and the lowest pressure is found at station 10. The highest pressures at the after body are 106.52 kPa, 92.58 kPa, 54.75 kPa, and 34.04 kPa at station 5A of models A, B, C, and D, respectively. Solving Eq. (8) yields a percentage difference of 15.7%, 6.2%, 31.3%, and 48.2%, which are less than the maximum pressure requirement of the floater design models A, B, C, and D, respectively.
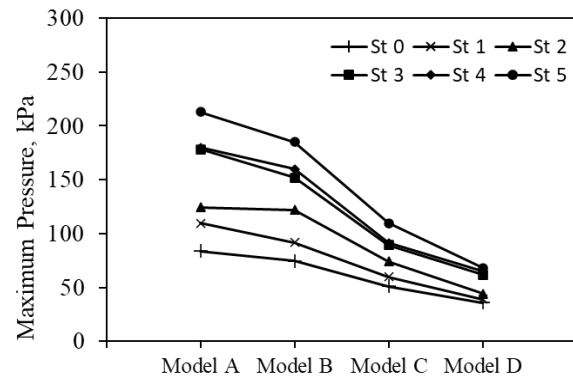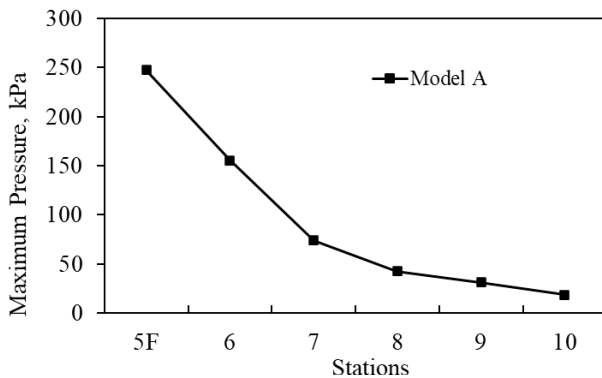

Fig. 10. Maximum pressure of model A in the fore body

Fig. 11. Maximum pressure at stations of the after body

Figure 11 depicts the maximum pressure at stations and discusses the implications of the deadrise angle caused by the afterbody's free-fall of all cross sections. At all stations, as the deadrise angle increases, the impact pressure decreases. The impact pressure reduces as the deadrise angle increases at all stations. The pressure differential between stations 0 and 5A varies; Fig. 11 indicates that models A, B, C, and D have cumulative maximum pressures of roughly 444.30 kPa, 392.65 kPa, 237.5 kPa, and 157.11 kPa, respectively, between stations 0 and 5A. This illustration shows how the inclusion of a deadrise angle causes pressure to be distributed more evenly across the afterbody longitudinally.

For the case of station 5A, the contour of the pressure phase in Fig. 12 depicts the interaction between models A, B, C, and D and the sea surface. The figures depict the maximum impact pressure caused by spray in the event that the body enters the water. The spray root area [11] had the highest pressure, and model A appears to have a significant spray, whereas model E's spray is not apparent enough due to the low impact pressure value.Table 3

Aries Sulisetyono, et a.I - Computational impact pressure of the floatplane's bottom in various of deadrise and flare angles

Journal of Applied Engineering Science- Vol.20, No 3, 2022 -www.engineeringscience.rs

shows the total maximum pressure of the afterbody region as determined using the Simpson formula for all models. The sum of the maximum pressures from stations 0 to 5A in model A is 444.30 kPa, which differs from models B, C, and D by 11.63 percent, 46.55 percent, and 64.64 percent, respectively.

Due to various initial speeds and heights during free-fall, the study explored differences in pressure values experienced by floatplane lower plates. The study results for model A at station 5A show that increasing the initial speed from 0 to 5 m/s results in a 54.97 percent increase in pressure values, with pressure magnitude of 106.52 kPa and 136.58 kPa, respectively. Figure 13 shows the pressure phase contour in the case of a 5 m/s initial speed, where the spray is higher than at 0 m/s. In other case, applying two vertical heights of 0.5 m and 1 m above the water surface to the free-fall body without initial speed provides results of roughly 106.52 kPa and 276.465 kPa, respectively. It demonstrates that by increasing the height by 0.5 m, the impact pressure on the body's bottom increases by around 61.47 percent. The pressure phase contours depict the difference between free fall from a height of 0.5 m and the 1 m seen in Fig. 14, which depicts the spray at a height higher than 0.5 m.
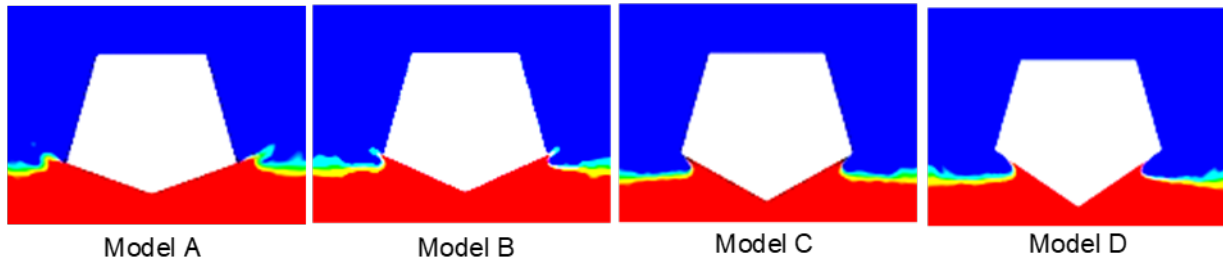

Fig. 12. Contour of pressure phase at station 5A

Table 3. The total pressure in the after body

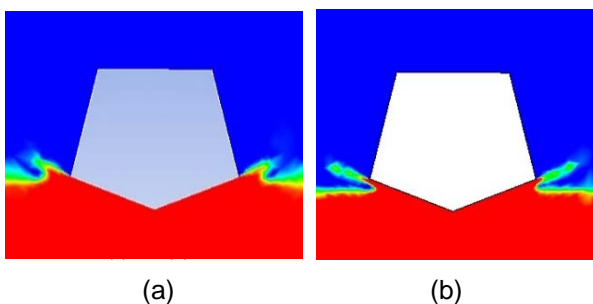| Angle Variation	Total Maximum Pressure (kPa)	Decrease
Model A	888.61	0.00%
Model B	785.29	11.63%
Model C	475	46.55%
Model D	314.22	64.64%

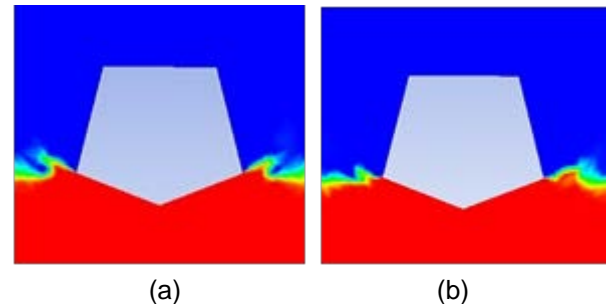Fig. 13. Pressure phase at initial speed of (a) 0 m/s and (b) 5 m/s in height of 0.5 m

Fig. 14. Pressure phase in initial height of (a) 0.5 m and (b) 1 m at initial speed of 0 m/s

The flare body effect is an increasing impact pressure since the hull flared (forebody) gives a lower impact pressure than the hull without flares (after body) (see Figs. 9 and 10). The forebody model A has various angles of the flares then converted into a body without flares by maintaining a wetted surface area, so that both are worth comparing. Models with and without flare, as shown in Fig. 7, are simulated free-fall into water, which gives the results in terms of impact pressure comparison between the two models. The forebody sections have various deadrise angles of about 20 to 48 degrees, and the flare angles are between 24 and 52 degrees (see Table 4). Table 4 shows some changes in maximum pressure on various parts ranging from 3.5 percent to 20.7 percent, implying that the flare can reduce impact pressure in general. The additional flare on the bottom design allows water forced against the water surface to easily flow due to the flare line's curved shape, resulting in comparatively modest spray.

Aries Sulisetyono, et al. - Computational impact pressure of the floatplane's bottom in various of deadrise and flare angles

Journal of Applied Engineering Science- Vol.20, No 3, 2022 -www.engineeringscience.rs

Table 4. Difference of unflared and flared models

Deadrise Angle(β)	Flare Angle(θ)	Maximum Pressure (kPa)		Difference (%)
		Unflared	Flared	
20°	24°	247.3	199.8	19.2
25°	30°	185.3	171	7.7
34°	37°	74.1	71.5	3.5
25°	30°	185.3	171	7.7
34°	37°	74.1	71.5	3.5
42°	45°	42.5	33.7	20.7
46°	50°	31	26.5	14.7
48°	52°	183.7	16.3	11.4

In comparison to Wagner's analytic equation adjustments, numerical simulation results using CFD prove their accuracy. Table 5 shows the percentage differences between the CFD and analytic results in this investigation. Both methods yield high impact pressure results. The deadrise angles of models A, B, C, and D are nearly identical in all circumstances (see Table 5). In certain conditions, some differences do not exceed 12%, and an average difference of about 5.16%, 5.21%, 4.75%, and 5.96% for the case of models A, B, C, and D, respectively. These differences are still acceptable so that both approaches are suitable for solving the free-falling body problem. However, solution with the Wagner equation is faster than CFD, but they will encounter difficulties in some cases of irregular and asymmetrical objects.

Table 5. Differences of CFD and Wagner's equation [12]

Station	Model			
	A	B	C	D
0	9.69%	8.54%	5.70%	4.84%
1	8.06%	3.75%	8.15%	1.85%
2	3.30%	3.24%	7.59%	2.45%
3	2.63%	8.00%	0.79%	6.16%
4	3.62%	4.60%	6.20%	11.69%
5A	2.99%	3.12%	0.08%	8.78%
5F	7.37%	-	-	-
6	7.39%	-	-	-
7	2.24%	-	-	-
8	0.94%	-	-	-
9	6.35%	-	-	-
10	7.35%	-	-	-

4 CONCLUSIONS

The impact pressure is calculated by simulating two dimensions of the floater's cross-section in free fall on the water surface. The effects of deadrise angles on the impact pressure body are studied using CFD modeling and four models with varying deadrise angles. The k-ε model is utilized in the CFD technique to deal with the water-free surface under the assumption of turbulent flow, utilizing the volume of fluid (VOF) approach.The approach's accuracy is confirmed by comparing it to a modified Wagner's equation that produces extremely similar results, with an average difference of roughly 5.3 percent of all models with an initial height of 0.5 m and no initial speed. The results reveal that the angle of deadrise influences the impact pressure of the floater's bottom region, with the maximum value of 247.3 kPa occurring at a deadrise angle of 20 degrees, i.e., Model A at station 5F, and pressure dropping as the deadrise angle was increased.By adding a flare that is roughly 3.5 percent to 20.7 percent lower than the unflared model, the pressure impact can be reduced. In the free fall scenarios, the initial height of 1 m and the initial speed of 5 m/s lead to the impact pressure being around 61.47 percent and 54.97 percent higher, respectively, than the 0.5 m initial height and 0 m/s initial speed.

5 ACKNOWLEDGMENTS

Aries Sulisetyono, et a.l - Computational impact pressure of the floatplane's bottom in various of deadrise and flare angles

Journal of Applied Engineering Science- Vol.20, No 3, 2022 -www.engineeringscience.rs

6 REFERENCES

[1] Sell, C. (2011). *Validation of Seaplane Impact Load Theory and Structural Analysis of the Martin 270*. M.S. Theses, Department School of Naval Architecture and Marine Engineering, University of New Orleans, New Orleans.

[2] F. A. A. (2004). *Seaplane, skiplane, and float/ski equipped helicopter operations handbook*. FAA-H-8083-23, Washington DC.

[3] Milwitzky, B. (1952). *Generalized theory for seaplane impact*. NACA Technical Report, no. 1103, NACA, USA.

[4] Karman, T. V. (1929) *The impact on seaplane floats during landing*. NACA Technical Note, no. 321, NACA, USA.

[5] Wagner, H. (1932). *The phenomena of impact and planing on water*. NACA Translation, no. 1366, NACA, USA.

[6] Chuang, S.L. (1996). *Slamming of rigid wedge-shaped bodies with various deadrise angle*. Technical Report DTMB-2268, DTMB Washington, USA.

[7] Dobrovol'skaya, Z.N. (1969). On some problems of similarity flow of fluid with a free surface. *Journal Fluid Mechanic*, vol. 36, no. 4, 805-829, DOI: 10.1017/S0022112069001 996

[8] Greenhow, M. (1987). Wedge entry into initially calm water. *Applied Ocean Research*, vol. 9, no. 4, 214-223, DOI: 10.1016/0141-1187(87)90003-4

[9] Korobkin, A.A., Pukhnachov, V.V. (1988). Initial stage of water impact.*Annual Review Fluid Mechanic*, vol. 20, 159-185, DOI: 10.1 146/annurev.fl.20.010188.001111

[10] Kapsenberg, G. K. (2011). Slamming of ships: where were we now?.*Philosophical Transactions of Royal Society A*, vol. 369, no. 1947, 2892-2919, DOI:10.1098/rsta.2011.0118

[11] Zhao, R., Faltinsen, O.M. (1993). Water entry of two-dimensional bodies. *Journal of Fluid Mechanic*, vol. 246, 593-612, DOI:10.1017/S002211209300028X

[12] Faltinsen, O.M. (2005). *Hydrodynamics of high-speed vehicles*. Cambridge University Press, UK.

[13] Yettou, E. M., Desrochers, A., Champoux, Y. (2007). A new analytical model for pressure estimation of symmetrical water impact of a rigid wedge at variable velocities. *Journal of Fluids and Structures*, vol. 23, no. 3, 501-522, DOI:10.1016/j.jfluidstructs.2006.10.001

[14] Dong, C., Sun, S., Song, H., Wang, Q. (2019). Numerical and experimental study on the impact between a free-falling wedge and water. *International Journal of Naval Architecture and Ocean Engineering*, vol. 11, no. 1, 233-243, DOI: 10.1016/j.ijnaoe.2 018.04.004

[15] Yu, P., Ong, M.C., Li, H. (2018). Effects of Added Mass and Structural Damping on Dynamic Responses of a 3D Wedge Impacting on Water. *Applied Science*, vol. 8, no. 5, 802, DOI: 10.3390/app8050802

[16] Wen, X., Liu, P., Qu, Q., Hu, T. (2020). Impact of wedge bodies on wedge-shaped water surface with varying speed.*Journal of Fluids and Structures*, vol. 92, 102831, DOI: 10.1016/j.jfluidstructs.2019.102831

[17] Wang, K., Ma, X., Bai, W., Lin, Z., Li, Y. (2021). Numerical simulation of water entry of a symmetric/asymmetric wedge into waves using OpenFOAM. *Ocean Engineering*, vol. 227, 108923, DOI: 10.1016/j.oceaneng.2021.108923

[18] Gudmundsson, S. (2021). *General Aviation Aircraft Design: Applied Method and Procedures 2nd Edition*, Elsevier Inc., Netherlands.

[19] Aliffrananda, M.H., Sulisetyono, A. (2021). Porpoising Instability Study of the Floatplane during Takeoff Operation on Calm Water. IOP Conference Series: Materials Science and Engineering, vol. 1052, 012013.

[20] Aliffrananda, M.H., Sulisetyono, A., Hermawan, Y.A., Zubaydi, A. (2022). Numerical analysis of floatplane porpoising instability at calm water during take-off. *International Journal Technology*, vol. 13, no. 1, 190-201, DOI: 10.14716/ijtech.v13i1. 4903

[21] Sulisetyono, A., Fadhlurrohman, I., Ali, B., Zubaydi, A. (2022). Computational prediction of the resistance of the the floatplane at various trim angles. Journal of Theoretical and Applied Mechanics, vol. 60, no. 2, 265 – 276, DOI: 10.15632/jtam-pl/148053

[22] Halliday, D., Resnick, R., Walker, J. (2021). *Fundamentals of physics 12th edition*. John Wiley & Sons, USA.

[23] Code of Federal Regulation (CFR). Aeronautics and space, from *https://www. ecfr.gov/current/title-14/chapter-I/subchapt er-C/part-25/subpart-C/subject-group-ECF R99790d9728306e9*, 2022-04-15.